Applied Catalysis B: Environmental 126 (2012) 265–274

Contents lists available at SciVerse ScienceDirect

Applied Catalysis B: Environmental

journal homepage: www.elsevier.com/locate/apcatb

Single-source precursor approach for the preparation of CdS nanoparticles and their photocatalytic and intrinsic peroxidase like activity

Swarup Kumar Maji[a], Amit Kumar Dutta[a], Supriya Dutta[b], Divesh N. Srivastava[c], Parimal Paul[c,*], Anup Mondal[a,*], Bibhutosh Adhikary[a,*]

[a] Department of Chemistry, Bengal Engineering and Science University, Shibpur, Howrah 711103, West Bengal, India
[b] Department of Chemistry, Budge Budge Institute of Technology, Budge Budge, Kolkata 700137, India
[c] Department of Analytical Sciences, Central Salt & Marine Chemicals Research Institute, Gijubhai, Badheka Marg, Bhavnagar 364002, Gujarat, India

ARTICLE INFO

Article history:
Received 1 December 2011
Received in revised form 25 June 2012
Accepted 16 July 2012
Available online 23 July 2012

Keywords:
CdS nanoparticles
Single-source precursor
Crystal structure
Photocatalytic activity
Peroxidase-like behavior

ABSTRACT

CdS nanoparticles (NPs) with different shapes and sizes (rods and spheres) have been synthesized through decomposition of a newly synthesized precursor complex $[Cd(SOCPh)_2Lut_2]$ using structure-directing solvents such as ethylenediamine (EN), dimethylsulfoxide (DMSO) and ammonia (NH_3). In addition, CdS NPs is also prepared by thermal decomposition of the precursor complex under N_2 atmosphere. The precursor complex is characterized by elemental analyses, TGA, FTIR, UV–vis spectroscopy and single crystal X-ray diffraction. The distorted tetrahedron geometry of the precursor complex has been determined by X-ray diffraction, which crystallizes in monoclinic crystal system of P2(1)/n space group with $a = 11.0487(17)$ Å, $b = 16.396(3)$, $c = 15.413(2)$ Å, $\alpha = 90.00^\circ$, $\beta = 109.708(4)^\circ$, $\gamma = 90.00^\circ$ and $Z = 4$. The CdS NPs are characterized using powder X-ray diffraction, transmission electron microscopy, BET analyses, UV–vis absorption and photoluminescence spectroscopy. The photo-catalytic activity of CdS NPs is studied by the degradation of Rose Bengal (RB) dye, indicating an excellent photocatalytic activity compared to that of commercial TiO_2. The mechanism behind photocatalytic degradation of RB in presence of CdS NPs is elucidated using terephthalic acid photoluminescence probing technique and evidence have shown that the photogenerated holes to be the predominant active species. This paper also demonstrates the intrinsic peroxidase like activity of CdS NPs toward peroxidase substrates 3,3′,5,5′-tetramethyl benzidine (TMB) and hydrogen peroxide. Kinetic analysis indicates that the catalysis by CdS NPs show typical Michaelis–Menten kinetics. Moreover, our synthesized CdS NPs show higher catalytic performances with a higher binding affinity for the substrate TMB than horseradish peroxidase (HRP) and other recently reported nano-mimitics.

1. Introduction

Organic dyes, phenolic compounds and their derivatives are commonly used in various and most of which are highly toxic and can remain in the environment in waste water for a long time [1]. Although a variety of physical, chemical and biological methods are used for treatment of waste water, majority of these processes are expensive and not highly effective [2]. In this regard, uses of semiconducting nanomaterials for degradation of organic pollutants have many advantages over other methods because of their environmental friendliness oxidation, mild reaction condition and low concentration usage [3]. TiO_2 is a well-known catalyst for photodegradation of toxic organic compounds; however, it is catalytically active only under UV irradiation because of its wide band gap energy [4]. Consequently, there is considerable demand for materials which are active in the visible region, since visible light is the main component in solar light and indoor illuminations [5]. Hence, alternate semiconductor nanomaterials as photocatalyst have been a topic of contemporary interest [6]. To this end, there are a lot of visible-light responsive photocatalysts such as ZnS, CdS, Bi_2S_3, In_2S_3, $CdIn_2S_4$, Fe_2O_3, Fe_3O_4, CuO, ZnO, MnO_2, Bi_2WO_6, $BiVO_4$ etc. have been reported in literatures [7–15]. In this work, we have chosen Rose Bengal (RB) dye to test the photoactivity, since it is a fluorescent dye and an important class of synthetic organic compound commonly used in textile, photographic and photochemical industries and therefore it is a common industrial pollutant. Few works have been made for the photocatalytic decomposition of RB in presence of semiconductor nanomaterials [16].

Moreover, peroxidases are the enzymes that typically catalyze the chemical reactions in a biological cell. The natural enzymes are efficient and higher specific biocatalyst under mild conditions.

* Corresponding authors. Tel.: +91 3326684561; fax: +91 3326682916.
E-mail addresses: anupmondal2000@yahoo.co.in (A. Mondal), bibhutoshadhikary@yahoo.in (B. Adhikary).

0926-3373/$ – see front matter © 2012 Elsevier B.V. All rights reserved.
http://dx.doi.org/10.1016/j.apcatb.2012.07.005

Due to their especial properties, natural enzymes also have significant applications in medicine, chemical industry, food processing and agriculture; however, it has some serious disadvantages [17]. In recent years, artificial enzymes have drawn prospective interest due to their simpler preparation, greater stability and effective efficiency over a wide range of pH and temperature. Mimetics of many natural enzymes have been developed and among them significant attention has been drawn on peroxidases, since it has potential applications in enzymatic analysis and also it is important for the waste water treatment [18]. Recently, it has been observed that different types of II–VI semiconductor nanomaterials show peroxidase-like activity [19–29]. However, how to develop a reproducible, environmental friendly and easier method to synthesize stable nanomaterials having good biological activity is still a challenge.

Cadmium sulfide, a direct band gap visible-light-sensitive II–VI group semiconductor (E_g = 2.41 eV) has been extensively studied as its optical properties can be tuned easily by changing the size and shape of the material [30]. It is useful for many important potential applications, such as light emitting diodes, flat panel displays, solar cell, photocatalyst, sensors, optoelectronic devices and thin film transistors [31–35]. Many synthetic methods have been employed for the preparation of CdS nanomaterials, but recently the single-source precursor approach has attracted considerable attention. It has the advantage of adopting a single-pot procedure under mild condition and the product obtained in this way has higher surface area, fewer defects and better stoichiometry. Several sulfur containing Cd(II) complexes have been used as precursors to synthesize variable shapes and sizes of CdS NPs under different conditions. The most widely used sulfur containing precursor complexes are the dithiocarbamato, dithiophosphinato, xanthate, thiohydrocarbazide, thiourea, thiocarboxylate, dithiocarrbazate and thiosemicarbazide [36–47]. Nyman et al. synthesized $Cd(SCOCR_2)_2Lut_2$ [R = CH_3,$C(CH_3)_3$, Lut = 3,5-dimethylpyridine (lutidine)] as the precursor complex for the preparation of spherical CdS NPs by thermal decomposition in toluene and pyridine [36]. Later, Yan et al. reported the preparation of quantum-confined CdS nanowires by the solvothermal decomposition of a cluster precursor $Cd_2(S_2CNEt_2)_4$ in presence of ethylenediamine as the nucleophile [47]. A $Cd(C_2H_5OCS_2)_2$ complex was synthesized by O'Brien et al. for the preparation of tri-n-octylphosphine oxide capped CdS NPs by solvothermal decomposition of the precursor complex [37]. Recently, Bera et al. developed a solvothermal single-source route for the bulk synthesis of CdS nanorods using a new dimeric cadmium(II) complex of S-benzyldithiocarbazate, $[Cd(PhCH_2SC(=S)NHNH_2)Cl_2]_2$ in hexamethylenediamine [46]. In majority of the cases they have used different nucleophilic solvents for the decomposition of precursors which are expensive and environmentally hazardous. In our case, we have shown that very commonly used, cheap laboratory reagents like NH_3, EN and DMSO, which are much less toxic, can be used for the preparation of CdS NPs. Additionally, we have shown that thermal decomposition of the precursor leads to the formation of CdS NPs, which has not been experimented by others.

In this work, we have tried to explore the effect of single-source molecular precursors on the morphology and size of the nanoparticles prepared from a newly synthesized Cd(II) thiocarboxylate complex. To the best of our knowledge, a simpler, greener and facial template-free method for the synthesis of CdS NPs has not been reported earlier. We demonstrate that the CdS NPs, either spherical or rod shape show remarkable photocatalytic efficiency toward the degradation of aqueous solution of RB in presence of white light and the kinetics of the decomposition process is also investigated. These CdS NPs exhibit good catalytic activity for the oxidation of TMB in presence of H_2O_2, by following the Michaelis–Menten kinetics.

2. Experimental

2.1. Materials

Reagent grade chemicals and solvents obtained from commercial sources were used as received. Standard titanium dioxide (Degussa-P25) was purchased from Degussa Company. Phosphate buffer solutions (PBS, 0.025 mol/L) with various pH were prepared by mixing standard solutions of Na_2HPO_4 adjusted the pH with H_3PO_4 or NaOH.

2.2. Synthesis of precursor complex

$CdCO_3$ (1.0 g, 3.8 mmol), 3,5-lutidine (0.82 g, 7.6 mmol) and 20 mL toluene were mixed in a round-bottom flask. Thiobenzoic acid (1.05 g, 7.6 mmol) mixed in 10 mL toluene was then added dropwise to the previous solution, with stirring. Within 30 min, a yellow suspension was obtained and the solvent was removed under reduced pressure after 2 h. The resulting yellow residue was re-dissolved in toluene and filtered. Filtrate was kept for slow evaporation in air for overnight. A good yellowish orange crystalline solid was collected by filtration.

Yield: 2.64 g (76%). $C_{28}H_{28}CdN_2O_2S_2$, Calcd: C, 55.89; H, 4.69; N, 4.66. Found: C, 55.84; H, 4.66; N, 4.63. FTIR (cm^{-1}): 3436 br, 3055 w, 2921 w, 1592 s, 1552 s, 1448 m, 1382 m, 1387 m, 1205 s, 11 677 s, 1034 w, 934 s, 863 w, 776 m, 695 s, 660 m, 545 w. UV/Vis [Chloroform, λ_{max}/nm (ε/M^{-1} cm^{-1})]: 275 (32 000). Crystal data: monoclinic, space group P2(1)/n; a = 11.0487(17) Å, b = 16.396(3) Å, c = 15.413(2) Å, α = 90.00°, β = 109.708(4)°, γ = 90.00°; V = 2628.7(7) $Å^3$; ρ = 1.519 g/cm^3; R1[a] = 0.0190; wR2[b] = 0.0422 [$I > 2\sigma(I)$] for 428 parameters and 5763 data.

2.3. Preparation of CdS NPs

2.3.1. Decomposition by heat treatment c.a. HT

1.0 g of $Cd(SOCPh)_2Lut_2$ was taken in a quartz boat and heated at 400 °C for 1 h in N_2 atmosphere, using a quartz tube furnace. The product was taken out after the furnace cooled down to room temperature. The color of the product changed to yellow after the thermal treatment.

2.3.2. Decomposition in EN

1.0 g of $Cd(SOCPh)_2Lut_2$ was dissolved in 20 mL EN in a round-bottom flask and then heated to reflux at 120 °C for 15 min. It was then cooled to room temperature and 20 mL methanol was added to it. The yellow suspension was centrifuged, followed by washing with methanol for several times for purification and then dried in air.

2.3.3. Decomposition in DMSO

1.0 g of $Cd(SOCPh)_2Lut_2$ was dissolved in 20 mL DMSO in a round-bottom flask and then heated at 120 °C for 15 min. The pure nanomaterial was then collected as mentioned in the earlier section.

2.3.4. Decomposition in NH_3

1.0 g of $Cd(SOCPh)_2Lut_2$ was dissolved in 50 mL of NH_3 in a conical flask and kept undisturbed at room temperature (300 K) for 12 h. A yellowish product was then collected following the above mentioned procedure.

2.4. Physical measurements

Elemental analyses (C, H and N) were carried out by a Perkin-Elmer 2400II instrument. Mass spectroscopic measurement was carried out on an Agilent Quadrupol LC–MS 6120 series mass

spectrometer. Thermogravimatric analysis was carried out by a Perkin-Elmer USA Diamond-200 measurement setup. XRD patterns were made on a Philips PW 1140 parallel beam X-ray diffractometer. X-ray structure was solved using with Bragg–Bretano focusing geometry and monochromatic CuK_α X-radiation (λ = 1.540 598 Å). TEM images were collected by using JEOL JEM-2100 microscope working at 200 kV. BET isotherms were obtained using a Quantachrome Instruments adsorption (77 K). FTIR spectra were recorded on a JASCO FTIR-460 Plus spectrophotometer. UV–visible absorption spectra were observed on a JASCO V-530 UV-vis spectrophotometer. Photoluminescence spectra were recorded using a Photon Technology International Fluorometer. The oxidation of TMB was monitored spectrophotometrically using an Agilent 8453 diode-array spectrophotometer.

2.5. Single crystal X-ray diffraction data

Crystals suitable for structure determinations of the molecule were obtained from slow evaporation of the compound solution in toluene. The crystals were mounted on glass fibers using perfluoropolyether oil. Intensity data were collected on a Bruker-AXS SMART APEX II diffractometer at 100(2) K using graphite monochromated MoKα radiation (λ = 0.710 73 Å). The data were processed with SAINT, and absorption corrections were made with SADABS [48]. The structures were solved by direct and Fourier methods and refined by full-matrix least-squares methods based on F^2 using SHELX-97 [49]. For the structure solutions and refinements, the SHELX-TL software package was used [50]. The non-hydrogen atoms were refined anisotropically, while the hydrogen atoms were placed at geometrically calculated positions with fixed thermal parameters. Crystallographic data, relevant bond lengths (Å) and angles (°) for the $Cd(SOCPh)_2Lut_2$ complex are given in supporting information.

2.6. Photocatalytic activity measurement

40 mL aqueous solutions of RB (3.6×10^{-5} M) was subjected to light irradiation in absence or presence of 15 mg of the catalysts at 20 °C. The suspensions were kept in dark for 30 min to reach the adsorption–desorption equilibrium. The irradiation was made with an incandescent tungsten halogen lamp (200 W) placed vertically at a distance of ca. 15 cm. At given time intervals, 3 mL aliquot was withdrawn and centrifuged. The concentration of the filtrate was then analyzed by UV–vis spectral measurement. After each photocatalytic test CdS NPs was collected by centrifugation followed by the heat treatment at 60 °C for 30 min and then it was reused for the next cycle.

Terephthalic acid (TA) photoluminescence probing technique was adopted to understand the mechanism of the photodegradation of RB by CdS NPs [7–12]. 40 mL aqueous solution of sodium terephthalate (2×10^{-3} M) containing 15 mg of either commercial TiO_2 or CdS NPs was irradiated with light for a given period of time. An aliquot (3 mL) from the suspension was withdrawn and centrifuged and its luminescence spectrum of was recorded between 350 and 600 nm using 315 nm as the excitation wavelength.

2.7. Peroxidase-like activity measurements

The catalytic experiments of the CdS NPs were carried out with 3 mL sodium acetate buffer (pH 4) containing H_2O_2 (13 mM) and TMB (0.1 mM) in absence and presence of CdS NPs (24 μg). The optimal conditions were established by varying the pH (2–10) and temperature (20–80 °C), respectively. In the comparative experiment, 3 mL sodium acetate buffer solution containing 0.1 mM of TMB and 13 mM of H_2O_2 was subjected to a series of experiments by adding (a) 24 μg of CdS obtained from HT (b) 24 μg of CdS obtained from EN (c) 24 μg of CdS obtained from DMSO and (d) 24 μg of CdS obtained from NH_3. The kinetic analyses were carried out by using 24 μg of CdS obtained from HT, a fixed amount of H_2O_2 (13 mM), and different amounts (0, 8, 16, 29, 35, 41, 54, 75, 91, 116 μM) of TMB solution; 24 μg of CdS obtained from HT, a fixed amount of TMB (0.1 mM) and different amounts (0, 6.5, 10, 16, 19, 23, 26, 32, 39, 45 mM) of H_2O_2 solution. The kinetic parameters were calculated using the Michaelis–Menten model [21].

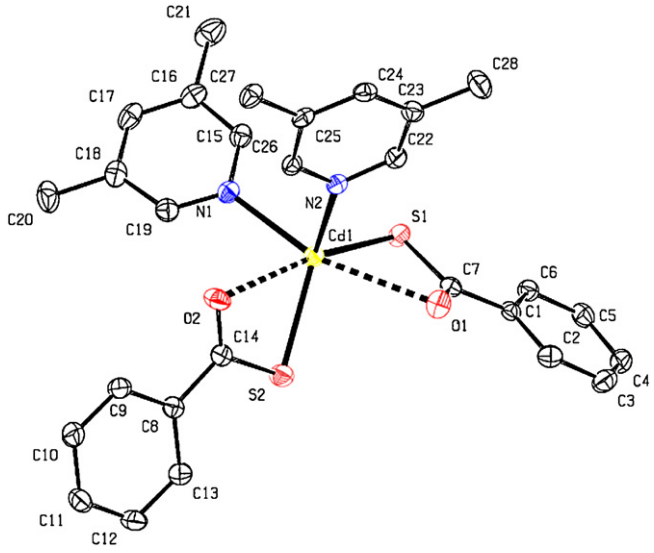

Fig. 1. ORTEP diagram of the single-source precursor complex $[Cd(SOCPh)_2Lut_2]$.

3. Results and discussion

The precursor complex $[Cd(SOCPh)_2Lut_2]$ was successfully synthesized by reacting cadmium carbonate with 3,5-lutidine and thiobenzoic acid (1:2:2) in toluene. The result of elemental analyses for the complex is in good agreement with the theoretical requirements of the composition. The FTIR spectrum for $Cd(SOCPh)_2Lut_2$ shows the presence of characteristic bands at 1592 cm^{-1} and 934 cm^{-1} (Supporting information, Fig. S1), which are assigned to the uncoordinated ν(C=O) in thiobenzoate and the ν(C—S), respectively. The electronic spectrum of the precursor shows a broad absorption bond at around 275 nm, which may be due to the intraligand transition. The chemical reaction that may be involved in this process can be written as

$$CdCO_3 + 2Lut + 2PhCOSH \rightarrow Cd(SOCPh)_2Lut_2 + CO_2 + H_2O \quad (1)$$

3.1. Solid-state structures of $Cd(SOCPh)_2Lut_2$

The molecular structure of the precursor complex was determined by single-crystal X-ray diffraction technique and the image is shown in Fig. 1. The molecule crystallizes in a monoclinic crystal system with P2(1)/n symmetry and four molecules are present in a unit cell. The two nitrogen atoms from lutidine and two sulfur atoms from thiobenzoate ligands are bonded to the central metal ion to provide a distorted tetrahedron CdN_2S_2 coordination environment. The distances between both Cd—O_1 (2.7844 Å) and Cd—O_2 (2.8018 Å) bonds are substantially longer than normal Cd—O distance, but shorter than the van der Walls radii, which indicates a weak interaction between the two atoms. Each unit cell contains four $Cd(SOCPh)_2Lut_2$ coordination units (Supporting information, Fig. 2a). The interesting structural feature of this compound is the presence of two types of face-to-face

aromatic π stacking interactions. First one is between the lutidine ring N(1)C(15)C(16)C(17)C(18)C(19) and the phenyl ring C(1) C(2) C(3) C(4) C(5) C(6) and the distance between two centroid is 3.707 Å. The second one is between two lutidine rings of N(2)C(22)C(23)C(24)C(25)C(26) and the distance between two centroid is 3.427 Å. These two types of π stacking interactions give rise to a three dimensional polymeric chain (Supporting information, Fig. 2b). The geometry around the metal is somewhat similar to the monomer, $Cd(SOCPh)_2(2,2'\text{-bpy})$ reported by Vittal et al. [43]. The variation in the two Cd—S (0.0511 Å) and two Cd—N (0.0773 Å) bond lengths are more than the variation obtained by Vittal et al., who have used 2,2′-bipyridine (bpy) instead of 3,5-lutidine. This is probably due to the presence of two lutidine rings which influence more geometrical distortion in $Cd(SOCPh)_2Lut_2$.

3.2. Thermogravimatric analysis of $Cd(SOCPh)_2Lut_2$

The thermal behavior of the precursor complex was studied by thermogravimatric analysis, carried out under N_2 atmosphere in the temperature range of 25–400 °C at a rate of 10 °C/min (Supporting information, Fig. S3). The result indicates that decomposition of the precursor starts at above 85 °C, giving 24.62% residue at 350 °C and results the formation of CdS, which is in good agreement with the calculated weight loss (24.04%). The curve shows two pronounced weight loss steps in between 85–230 °C and 230–350 °C, respectively. The first weight loss (41.17%) is due to the decomposition of the $S(OCPh)_2$ group (calc. wt% = 40.6), and the suggested product is $CdSLut_2$. While in the second step, $CdSLut_2$ is decomposed to CdS by the elimination of two lutidine group, with calculated and measured weight loss of 34.23% and 35.65%, respectively. This formation of CdS is also supported by the powder X-ray diffraction pattern of the residue obtained from the TGA pan. The formation of pure crystalline CdS in the solid-state thermal decomposition process of $Cd(SOCPh)_2Lut_2$ suggests that this is the reasonable precursor to the metal sulfide. The possible steps for the decomposition of $Cd(SOCPh)_2Lut_2$ to CdS are shown below.

$$Cd(SOCPh)_2Lut_2 \rightarrow CdSLut_2 + S(OCPh)_2 \quad (2)$$

$$CdSLut_2 \rightarrow CdS + 2Lut \quad (3)$$

3.3. Characterizations of CdS NPs

The purity and crystallinity of CdS NPs were first examined using powder XRD measurements and the diffraction patterns are shown in Fig. 2a–e. The diffraction peaks can be clearly indexed to the cubic and hexagonal phases of CdS, which is in good agreement with the literature results (JCPDS Card 42-1411 and 41-1049). It can be pointed out that, we could selectively prepare cubic and hexagonal phases of CdS from the same precursor complex depending upon the reaction parameters. Any significant characteristic peaks of other impurities are not detected in the diffraction pattern, suggesting the purity of the prepared materials. The patterns show peak broadening, which indicates the formation of nanoparticles. From Fig. 2b, it can be seen that the (0 0 2) diffraction peak is narrow and strong, indicating a preferential growth along the *c* axis, which is in good agreement with TEM result. Crystallite size (*D*) for the prepared materials were calculated using the Debye–Scherrer equation ($D = 0.9\lambda/(\beta\cos\theta)$), where, *D* is the crystallite size, λ is the wave length of X-ray (1.540 598 Å), β is the value of full width at half maximum and θ is the Bragg's angle. Using this equation, the crystallite sizes were calculated and have been presented in Table 1.

Morphological investigations of CdS NPs were made by TEM measurements and the obtained results are displayed in Fig. 3a–d and Table 1. It can be observed that the morphologies and sizes of the prepared CdS NPs highly depend on the solvents and applied conditions. The obtained CdS NPs looks like rod (hexagonal crystallite) when EN was used as the solvent (120 °C for 15 min), which is in good agreement with XRD pattern (Fig. 3b). When DMSO and

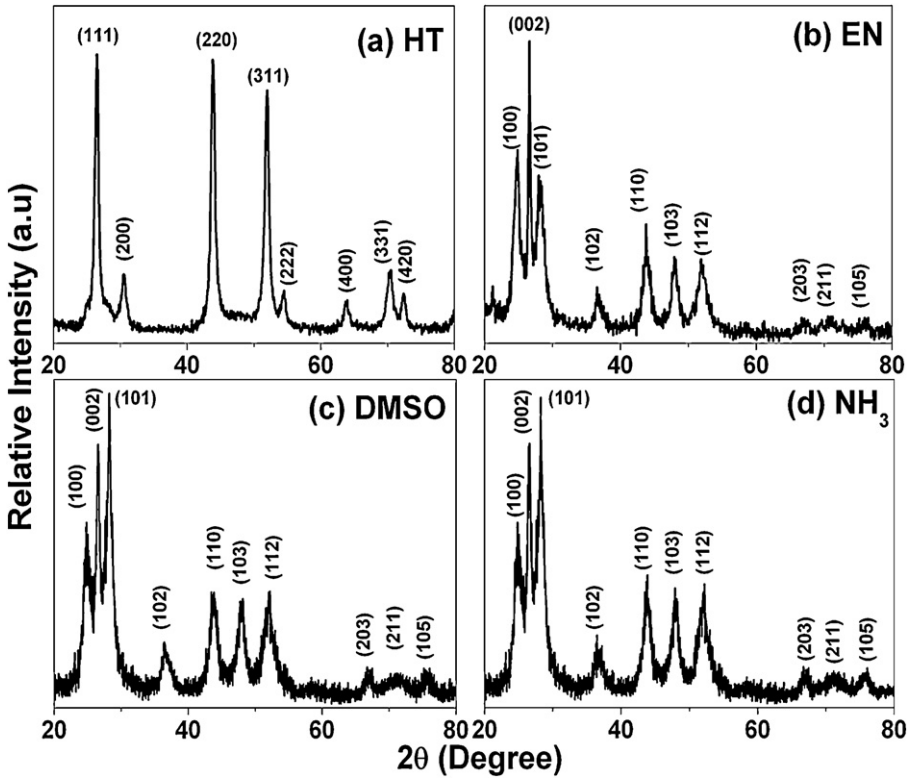

Fig. 2. XRD patterns for CdS NPs obtained from (a) HT, (b) EN, (c) DMSO and (d) NH_3.

Table 1
Summary of reaction conditions and experiments results.

Reactants	Temp (°C)	Time	Shape	Average size (nm)		Average pore diameter (nm)	Specific surface area ($m^2\ g^{-1}$)
				XRD	TEM		
Precursor	400	1 h	Spherical	6.7	10	4.5	57.3
Precursor + EN	120	15 min	Rod	5.1	$D = 6$[a], $L = 25–100$[b]	3.8	43.2
Precursor + DMSO	120	15 min	Sphere	3.8	4	2.9	33.1
Precursor + NH_3	27	12 h	Sphere	3.86	4	2.2	26.6

[a] Diameter.
[b] Length.

NH_3 were employed as solvents (120 °C for 15 min and 27 °C for 12 h), both the CdS NPs show spherical morphology (hexagonal crystallite), as displayed in Fig. 3c and 3d. Moreover, in case of direct annealing of the precursor, it also gives nanospheres of larger size than that of DMSO and NH_3, with cubic crystallite (Fig. 3a). Moreover, several types of CdS NPs have been obtained from the same precursor complex by changing the reaction conditions. The average particle sizes as observed from the TEM images are similar to the results of XRD measurements for CdS NPs obtained from EN, DMSO and NH_3. Where as, due to some aggregation of CdS NPs obtained from HT, a slightly higher value is obtained for the TEM image than the XRD result. Further information about the microstructure of the CdS NPs was provided by their SAED patterns and HRTEM images. The SAED patterns for each sample are given in their insets of TEM image (Fig. 3), which suggest the small and polycrystalline nature of the materials. The diffraction planes are obtained from the SAED patterns match well with the XRD patterns. HRTEM images show the structurally uniform lattice fringes of nanocrystals (Fig. 3, insets), suggesting the good crystalline nature of the prepared materials. The measured fringe spacing of 0.21 (CdS from HT), 0.323 (CdS from EN), 0.33 (CdS from DMSO) and 0.31 nm (CdS from NH_3) correspond to the separation of the (2 0 0), (0 0 2) and (1 0 1) lattice planes, respectively.

BET (Brunauer–Emmett–Teller) isotherm measurements were carried out under N_2 atmosphere to know the porous nature of CdS NPs. Mesoporous nature for all CdS NPs is established (type IV isotherm) from the BET plots (Supporting information, Fig. S4). The increase in the nitrogen uptake and a small hysteresis loop at relative pressures in the range of 0.8–1.0 in the isotherm is generated due to the capillary condensation of the absorbate in the mesopores of the solid. The average pore diameters were calculated by the Bopp–Jancso–Heinzinger (BJH) method (Supporting information, Fig. S4 inset), which shows the average pore diameters are in the range of 2.2–4.5 nm. The specific surface areas were also calculated and are found to be in the range of 26.6–57.3 $m^2\ g^{-1}$ (Table 1).

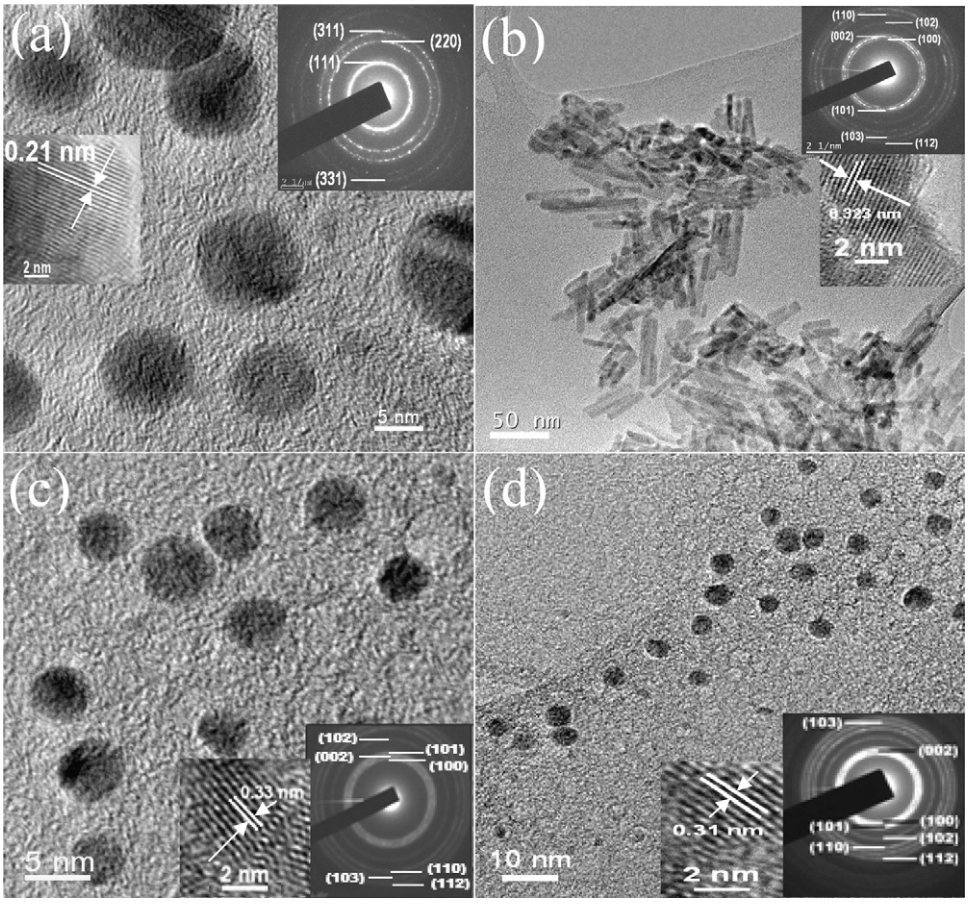

Fig. 3. TEM images (inset: corresponding SAED pattern and lattice fringe) for CdS NPs obtained from (a) HT, (b) EN, (c) DMSO and (d) NH_3.

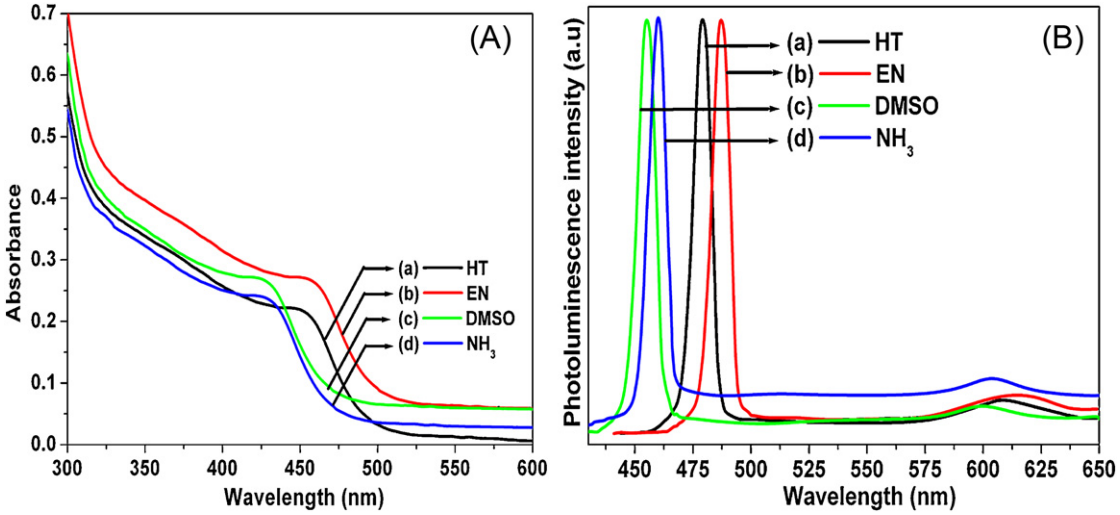

Fig. 4. Room temperature (A) UV–vis absorbance spectra and (B) photoluminescence spectra for CdS NPs obtained from (a) HT, (b) EN, (c) DMSO and (d) NH_3.

3.4. Formation mechanism of CdS NPs

The formation of different sizes of nanorods and nanospheres by decomposition of the precursor complex are well controlled under various reaction conditions. The precursor complex $[Cd(SOCPh)_2Lut_2]$, would be unstable in presence of nucleophiles and under thermal condition. Nucleophilic attack by nucleophilic solvents at the thione carbon and by thermal decomposition of the precursor can lead to the formation of $[CdS]_2$ crystal nuclei [47]. The newly generated $[CdS]_2$ crystal nuclei are highly active and have tendency to combine with each other to grow into larger nanocrystals. During the crystal growth process, these $[CdS]_2$ crystal nuclei may preferentially grow along a unique direction into nanorods or aggregate into quasi-spherical or irregular structures depending upon the solvents and reaction conditions. When nucleation starts, the coordinating solvents are also adsorbed on the surfaces of CdS crystal nuclei and form the corresponding complexes with Cd^{2+} ions [CdS(L)*n*, L = nucleophilic solvent; *n* = number]. As a strong bidentate chelating ligand, EN binds to the nonpolar facets of the nucleus leaving the polar (0 0 2) facets open, in which direction growth of nanoparticles can take place resulting in the nanorods. However, in case of DMSO and NH_3, they fail to form such anisotropic capping of the CdS nuclei, but symmetrically cap all the faces of the nuclei leading to the formation of thermodynamically stable quasi-spherical CdS NCs. When the precursor was annealed at 400 °C, due to absence of such types of capping, the energetically unfavorable CdS nuclei combine with each other to grow into larger quasi-spherical nanoparticles.

3.5. Optical properties of CdS NPs

Fig. 4A is the room temperature UV–vis absorption spectra for CdS NPs dispersed in water. The spectra show sharp band edge absorptions in between 470 nm and 500 nm with a well defined absorption feature with absorption maximum at around 422–455 nm. The well resolved absorption maxima correspond to the first optically allowed transition between the electron and the hole and also suggest the monodispersive nature of the samples [47]. The band gap energies were estimated from their absorption peaks and are found to be 2.76 (CdS from HT), 2.73 (CdS from EN), 2.94 (CdS from DMSO) and 2.92 eV (CdS from NH_3). The band gap energies are considerably blue shifted due to the quantum confinement effect by an amount of 0.32–0.53 eV, compared to that of bulk CdS (2.41 eV) [37,51]. The amount of blue-shift is different for different CdS NPs, since more is the reduction in crystallite size, higher will be the amount of blue shifted energy. Therefore, the wavelength of the absorption peak can be tuned by changing the reaction conditions at the decomposition step of the precursor. From the absorption maxima (λ_{max}), the average particle size can be calculated [52] and are found to be 5.27 (CdS from HT), 5.49 (CdS from EN), 4.1 (CdS from DMSO) and 4.2 (CdS from NH_3), which are consistent with the results from the TEM and XRD measurements.

The photoluminescence properties of CdS NPs were investigated at room temperature with an excitation wavelength of 375 nm and are shown in Fig. 4B. The spectra show strong and sharp typical direct electron–hole recombination [53] between 455 nm and 487 nm with a broad emission at ca. 600 nm. The emission peaks are also blue shifted from bulk CdS due to the quantum confinement effect [54]. The high intensity of the band-edge emission confirms the high state of crystallinity with few electronic defects and the good dispersity of nanomaterials [55]. The additional broad red emission in photoluminescence spectra at ca. 600 nm corresponds to the recombination of trapped electrons and holes in some surface defect states of CdS NPs [39,56].

3.6. Photocatalytic activity by CdS NPs

Photocatalytic activities of CdS NPs were evaluated by the degradation of RB in aqueous solution under white light illumination. As shown from the time-dependent UV–vis absorption curves of RB solution catalyzed by CdS NPs obtained from HT (Fig. 5a), the absorption intensity of RB at 554 nm decreases rapidly and completely disappears after 55 min. During the reaction, no new peaks are generated, whereas, the absorption intensities at 350, 305, 255 and 212 nm decrease, suggesting the complete photodegradation of RB rather than decolorization or bleaching [16c]. To establish the enhanced photocatalytic activity of synthesized CdS NPs a comparative study was carried out with commercial TiO_2 as reference and the relative concentration vs. time plots are shown in Fig. 5b. The stock solution of RB (3.6×10^{-5} M) was divided into eight parts and experiments were carried out under the conditions of (i) without catalyst in dark (ii) without catalyst in light, (iii) CdS NPs from HT (15 mg) in dark, (iv) TiO_2 (15 mg) in light, (v) CdS NPs from HT (15 mg) in light, (vi) CdS NPs from EN (15 mg) in light, (vii) CdS NPs from DMSO (15 mg) in light and (viii) CdS NPs from NH_3 (15 mg) in light. After 55 min of light illumination, the degradation of RB was achieved up to 99.1% (Fig. 5b, condition v) by the use of CdS

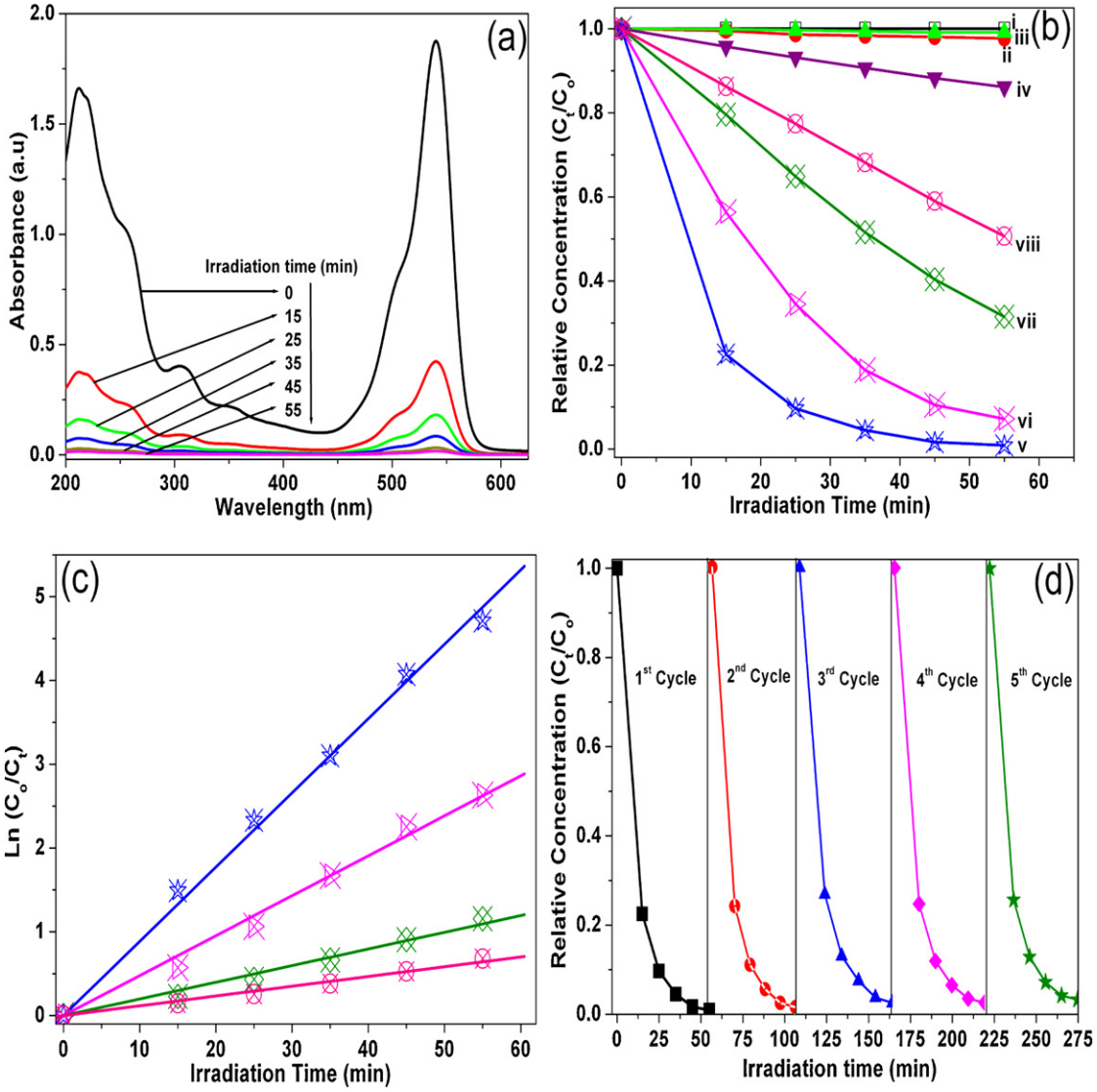

Fig. 5. (a) The time-dependent UV–vis absorption spectral changes of aqueous RB solution catalyzed by CdS NPs from HT under light irradiation, (b) degradation of RB in terms of relative concentration vs. time plots under different conditions, (c) kinetic plots for the photodegradation process of RB catalyzed by CdS NPs and (d) cyclic run for the catalytic decomposition of RB with CdS NPs (from HT).

NPs from HT, however, the decomposition of RB by commercial TiO_2 under same condition was only 13.8% (Fig. 5b, condition iv). This result suggests that our synthesized CdS NPs have excellent photocatalytic activity compared to commercial TiO_2. To know the effect of catalysis and photolysis, we have also carried the degradation of RB with and without catalyst in dark and with catalyst in light (Fig. 5b, conditions iii, i and ii), and the experiments suggest that the decomposition of RB is due to the photolysis by CdS NPs. Among the four types of CdS NPs, that obtained from HT shows the highest activity (99.1%), which then decreases from EN (92.8%) to DMSO (68.5%) to NH_3 (49.3%), but are still better than that of TiO_2. The relative smaller size, larger surface area and high crystallinity of nanoparticles may be a key factor for the enhance photocatalytic degradation of RB. The reaction rates for the photocatalytic decomposition of RB were determined using the pseudo-first order reaction kinetics: $\ln(C_o/C_t) = kt$, where, C_o represents the initial concentration, C_t denotes the concentration at a given reaction time "t", and k is the reaction rate constant. The reaction rate constants are obtained from the $\ln(C_o/C_t)$ vs. t plots (Fig. 5c) and are found to be 8.9×10^{-2} min^{-1} (CdS from HT), 4.8×10^{-2} min^{-1} (CdS from EN), 2.0×10^{-2} min^{-1} (CdS from DMSO) and 1.6×10^{-2} min^{-1} (CdS from NH_3). The Photocatalytic activity of the samples is found to be in the order of CdS NPs obtained from HT > EN > DMSO > NH_3. The activity order can be ascribed to the increase in specific surface area and crystallinity of CdS NPs obtained from NH_3 to DMSO to EN to HT.

The most important factor for the practical utility of a photocatalyst is its reusability and stability during the course of illumination. CdS NPs were recycled and reused successively for three times for the decomposition of RB under identical experimental condition (Fig. 5d). After five successive recycles the catalyst does not exhibit any significant loss of activity, indicating that the nanoparticles are relatively stable and not photocorroded during the photocatalytic process. The XRD pattern and TEM image acquired after photolysis (Supporting information, Fig. S5) illustrate that there are no structural changes of the NPs. This establishes the stability of the synthesized CdS NPs.

The complete decoloration of the dye solution does not necessarily mean the total decomposition of the dye molecules. In fact, decoloration may also occur due to photo-bleaching. However, we have established here, that the photodecomposition of the dye really occurs in presence of CdS NPs, by investigating the

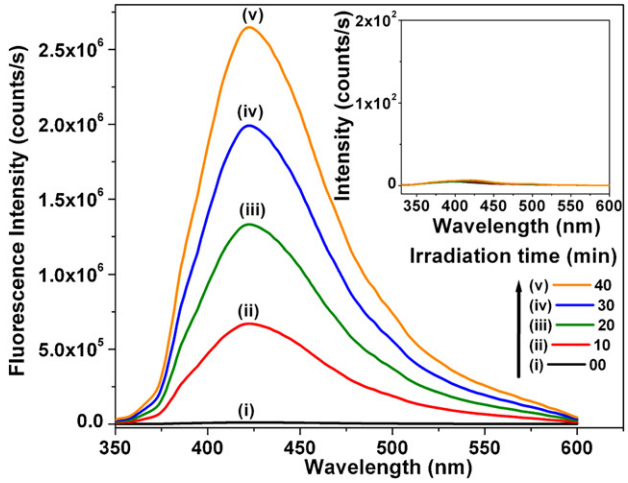

Fig. 6. Photoluminescence spectral changes of terephthalic acid solution with commercial TiO_2 and CdS NPs obtained from HT (inset).

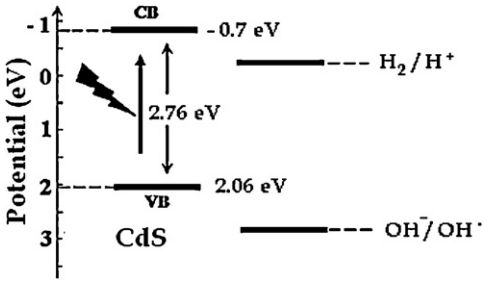

Fig. 7. Schematic illustration for energy bands of CdS NPs and normal potentials of H_2/H^+ and $OH^-/\bullet OH$ couple.

colorless solution through LC–MS study. The mass spectrum (Supporting information, Fig. S6) did not show any peak for high molecular weight compounds. A significant peak could only be observed at $m/z = 113.1$, which corresponds to the chlorobenzene group, indicating the total breakage of the Rose Bengal molecule into very small fragments. Therefore, it can be concluded that a

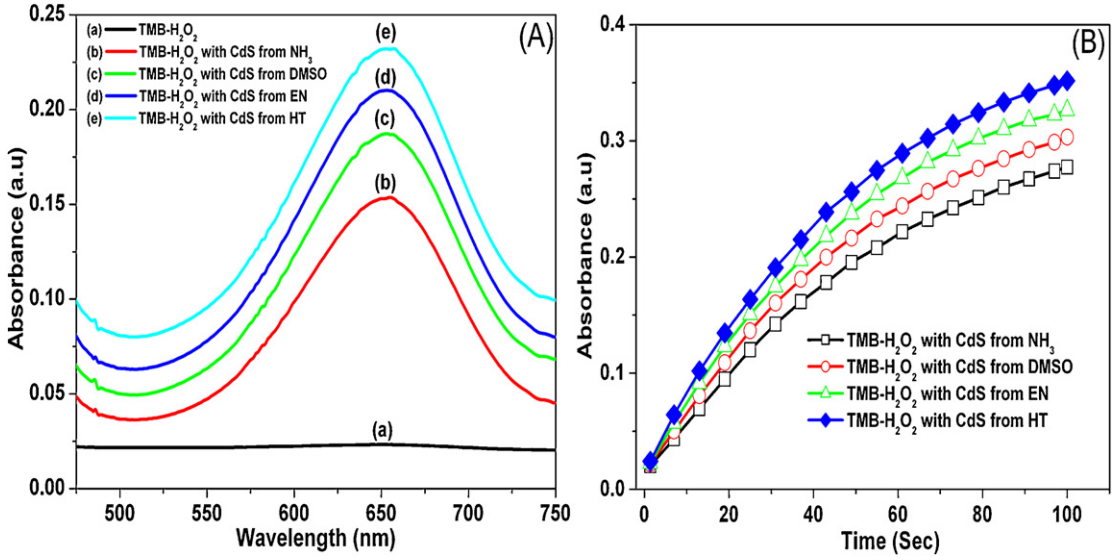

Fig. 8. (a) UV–vis absorption curve of TMB–H_2O_2 solution system under different conditions and (b) time-dependent catalytic activity of different CdS NPs with TMB and H_2O_2 as substrates under the optimized conditions.

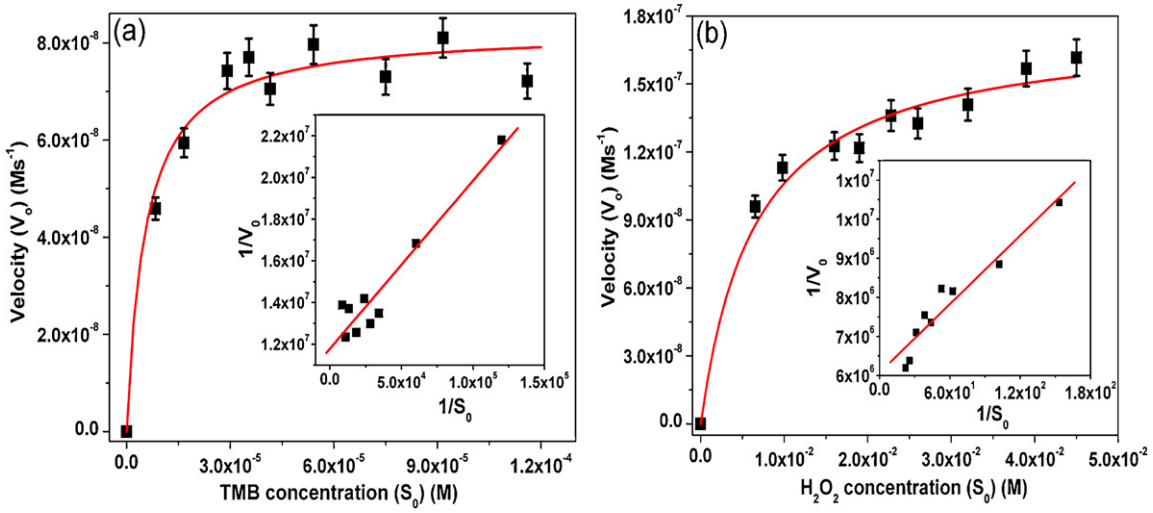

Fig. 9. Steady-state kinetic analyses using Michaelis–Menten model and Lineweaver–Burk model (insets) for CdS NPs (obtained from HT) by (a) varying the concentration of TMB with fixed amount of H_2O_2 and (b) varying the concentration of H_2O_2 with fixed amount of TMB.

complete decomposition of Rose Bengal has been achieved using CdS NPs as a photocatalyst under light illumination.

The mechanism for the photo-degradation of RB by CdS NPs has been studied using the terephthalic acid photoluminescence probing technique. It is well established that photodegradation catalyzed by TiO_2 involves the generation of hydroxyl radical (•OH), which can be observed by the increasing photoluminescence intensity at 422 nm due to the formation of strong fluorescent molecule 2-hydroxylterephthalic acid (HTA) (Fig. 6) [7–12]. With CdS NPs, no significant luminescence could be observed even on strong exposure to light, suggesting the lack of •OH radical generation (Fig. 6, inset). The above results show that the •OH radicals are not the main active oxygen species in the photocatalytic degradation of RB on CdS. This can be explained by the location of valence band of CdS and the normal potential of OH^-/•OH couple (2.7 eV vs. SCE). The conduction band (CB) and valence band (VB) potentials of the semiconductor at the point of zero charge are calculated by the following equation [14]:

$$E_{VB} = X - E_e + 0.5E_g \quad (4)$$

where X is the absolute electronegativity of the semiconductor (ca. 5.18 eV), E_e is the energy of free electrons on the hydrogen scale (ca. 4.5 eV), E_{VB} is the VB edge potential and E_g is the band gap of the semiconductor. The conduction band position can be deduced by $E_{CB} = E_{VB} - E_g$. The position of valence band and conduction band were calculated to be 2.06 and −0.7 eV, respectively (Fig. 7). Due to more positive value of VB edge potential for OH^-/•OH couple, the photogenerated holes on the surface of CdS cannot react with OH^-/H_2O to form •OH. On the basis of theoretical aspects and experimental results, it can be concluded that the degradation of RB in presence of CdS NPs is due to the direct participation of photogenerated holes.

3.7. Peroxidase-like behavior of CdS NPs

In order to investigate the peroxidase-like activity of CdS NPs, the catalytic oxidation of a peroxidase substrate as TMB has been studied in presence of H_2O_2. The colorless TMB solution, catalyzed by CdS NPs turns blue in presence of H_2O_2, which can be quenched by the addition of H_2SO_4 to produce a yellow color (Supporting information, Fig. S7). The reaction was monitored by following the increase of absorbance at 653 nm with time as shown in Fig. 8a, which originated from the oxidation product of TMB, similar to the phenomenon observed for the commonly used horse radish peroxidase enzyme [19]. The effects of pH and temperature on the oxidation of TMB were investigated in the pH range 2–10 and the temperature 20–80 °C. From the response curves (Supporting information, Fig. S8), the optimized catalytic conditions are approximately pH 4.0 and temperature 40 °C.

To find out the activity order among the four types of CdS NPs, a comparative study was carried out under the optimized catalytic conditions. Fig. 8b shows the time-dependent catalytic activity of different CdS NPs measured for 100 s, which show different level of activity over the reaction time, in the order of CdS NPs obtained from HT > EN > DMSO > NH_3, similar to that of photocatalytic decomposition of RB. The activity order is same in both cases, since both the properties are directly related to the porosity factor.

The apparent steady-state reaction kinetic parameters by initial rate method were determined to investigate the mechanism of the peroxidase-like activity of CdS NPs. In this case we have determined the kinetic parameters of the CdS catalyst prepared from HT, since it has the highest catalytic activity among them. Apparent steady-state reaction parameters at different concentrations of substrate were obtained by calculating the slopes of initial absorption changes with time. As shown in Fig. 9a and b, the curves

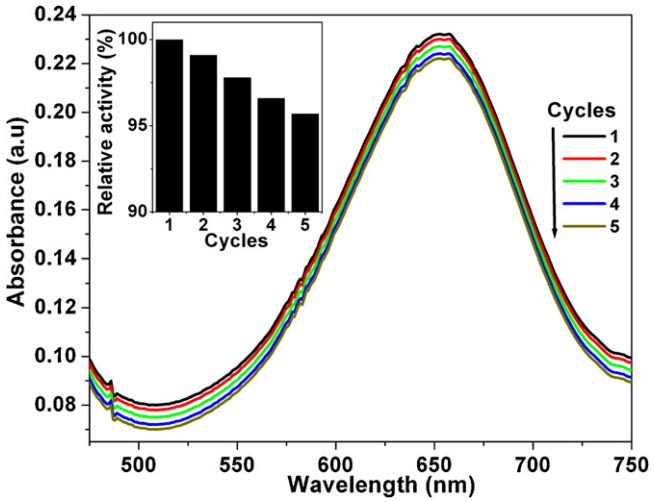

Fig. 10. The catalytic activity of CdS NPs from HT in five successive recycles. Inset: relative activity vs. number of cycles.

indicate the typical Michaelis–Menten kinetic for the oxidation of TMB by varying the concentration of TMB and H_2O_2, respectively. To determine the catalytic parameters, the data were fitted to the Michaelis–Menten equation and the obtained kinetic parameters are shown in Table 2. All the parameters were also calculated by the Lineweaver–Burk double-reciprocal plot ($1/V_0$ vs. $1/S_0$), which give analogous results and are shown in insets of Fig. 9a and b. The apparent Michaelis constant (K_m^{app}, which is the measure of enzyme affinity for its substrate), with TMB as substrate is 0.0054 mM, which is eighty times lower that that of HRP [19]. As compared to the HRP and other recently reported nano-mimetics [19–29], CdS NPs has the lowest K_m^{app}, suggesting the highest affinity toward TMB (Table 2). In contrast, the K_m^{app} of CdS NPs with H_2O_2 as the substrate is 6.54 mM, which is about double than that of HRP [19] and GO—COOH [27] (Table 2), suggesting that a higher H_2O_2 concentration is required to achieve the maximal activity for CdS NPs. However, the K_m^{app} with H_2O_2 as the substrate is significantly lower than that of other nano-mimetics [20,21,28,29] (Table 2), indicating the higher affinity to H_2O_2. These results indicate that our synthesized CdS NPs have intrinsic peroxidase-like activity and have good affinity to both TMB and H_2O_2, and therefore can be used as artificial peroxidases.

As we know that CdS NPs is an inorganic material, therefore it is expected to be more thermally and chemically stable than natural peroxidases. To investigate the stability and reproducibility of the catalytic activity of CdS NPs (from HT), it was recycled for five times. A small decrease in the absorption intensity is observed after five

Table 2
Apparent steady-state kinetic parameters for CdS NPs.

Catalyst	Substrate	K_m^{app} (mM)
CdS NPs	TMB	0.0054
	H_2O_2	6.54
HRP [19]	TMB	0.434
	H_2O_2	3.70
Fe_3O_4 MNPs [29]	TMB	0.098
	H_2O_2	154
FeS [20]	TMB	0.13
	H_2O_2	7.2
PBMNPs3 [21]	TMB	0.307
	H_2O_2	323.6
CuO NPs [28]	TMB	0.013
	H_2O_2	85.6
GO—COOH [27]	TMB	0.0237
	H_2O_2	3.99

successive cycles (Fig. 10), which indicates that CdS NPs are stable and exhibit excellent reproducibility in the cycling process.

4. Conclusion

In summary, CdS with nanorods and nanospheres have been prepared by one step decomposition of a newly synthesized precursor complex. The structure of the precursor $[Cd(SOCPh)_2Lut_2]$ has been determined by the single crystal X-ray diffraction. Structural and optical properties of CdS NPs were investigated and the correlations between shapes and sizes have been made. Using these nanomaterials, we have tried to investigate some proper applications in the field of environment and biochemistry. The CdS NPs show excellent photocatalytic degradation for organic pollutants (RB) for their probable application in waste water treatment. Peroxidase-like activity of them was also examined and suitable results as artificial peroxidases have been found.

Acknowledgements

Authors are thankful to Prof. K. Nag (IACS, Kolkata) for helpful discussion. S.K. Maji and A.K. Dutta are indebted to CSIR, India and UGC, India, for their SRF [08/003(0089)/2012-EMRI] and [11-2/2002 (SA-I)], respectively. Thanks to MHRD-India and UGC-SAP (India) for providing instrumental facilities to the Department of Chemistry, Bengal Engineering and Science University, Shibpur, India. Thanks are also to the Department of Inorganic Chemistry, Indian Association for the Cultivation of Science for providing X-ray crystallographic facility.

Appendix A. Supplementary data

Supplementary data associated with this article can be found, in the online version, at http://dx.doi.org/10.1016/j.apcatb.2012.07.005.

References

[1] L.H. Kieth, W.A. Telliard, Environmental Science & Technology 13 (1979) 416.
[2] Y. Bessekhouad, M. Mohammedi, M. Trari, Solar Energy Materials and Solar Cells 73 (3) (2002) 339.
[3] E. Forgas, T. Cserhati, G. Oros, Environment International 30 (2004) 953.
[4] Y. Chen, D. Dionysiou, Journal of Molecular Catalysis A: Chemical 244 (2006) 73.
[5] W. Zhao, C. Chen, X. Li, J. Zhao, H. Hidaka, N. Serpone, Journal of Physical Chemistry B 106 (2002) 5022.
[6] B. Lim, M.J. Jiang, P.H.C. Camargo, E.C. Cho, J. Tao, X.M. Lu, Y.M. Zhu, Y.N. Xia, Science 324 (2009) 1302.
[7] X. Yu, J. Yu, B. Cheng, B. Huang, Chemistry: A European Journal 15 (2009) 6731.
[8] J. Yu, G. Dai, B. Huang, Journal of Physical Chemistry C 113 (2009) 16394.
[9] J. Yu, J. Zhang, S. Liu, Journal of Physical Chemistry C 114 (2010) 13642.
[10] J. Yu, J. Zhang, M. Jaroniec, Green Chemistry 12 (2010) 1611.
[11] Y. He, D. Li, G. Xiao, W. Chen, Y. Chen, M. Sun, H. Huang, X. Fu, Journal of Physical Chemistry C 113 (2009) 5254.
[12] M. Sun, D. Li, W. Li, Y. Chen, Z. Chen, Y. He, X. Fu, Journal of Physical Chemistry C 112 (2008) 18076.
[13] J.S. Hu, L.L. Ren, Y.G. Guo, H.P. Liang, A.M. Cao, L.J. Wan, C.L. Bai, Angewandte Chemie International Edition 44 (2005) 1269.
[14] P. Madhusudan, J. Ran, J. Zhang, J. Yu, G. Liu, Applied Catalysis B 110 (2011) 286.
[15] G.M. Neelgund, A. Oki, Applied Catalysis B 110 (2011) 99.
[16] (a) X.Z. Li, H.L. Liu, P.T. Yue, Environmental Science and Technology 34 (2000) 4401;
(b) M.A. Rauf, N. Marzouki, B.K. Korbahti, Journal of Hazardous Materials 159 (2008) 602;
(c) Q. Chen, D. Jiang, W. Shi, D. Wu, Y. Xu, Applied Surface Science 255 (2009) 7918;
(d) S.K. Maji, N. Mukherjee, A. Mondal, B. Adhikary, Polyhedron 30 (2012) 145;
(e) S.K. Maji, A.K. Dutta, D.N. Srivastava, P. Paul, A. Mondal, B. Adhikary, Polyhedron 30 (2011) 2493.
[17] M.J. Banholzer, J.E. Millstone, L. Qin, C.A. Mirkin, Chemical Society Reviews 37 (2008) 885.
[18] (a) J. Zhang, M. Oyama, Electrochimica Acta 50 (2004) 85;
(b) W. Chen, B. Li, C. Xu, L. Wang, Biosensors and Bioelectronics 24 (2009) 2534;
(c) Q. Wang, Z. Yang, X. Zhang, X. Xiao, C.K. Chang, B. Xu, Angewandte Chemie 119 (2007) 4363.
[19] L. Gao, J. Zhuang, L. Nie, J. Zhang, Y. Zhang, N. Gu, T. Wang, J. Feng, D. Yang, S. Perrett, X. Yan, Nature Nanotechnology 2 (2007) 577.
[20] Z. Dai, S. Liu, J. Bao, H. Ju, Chemistry: A European Journal 15 (2009) 4321.
[21] X.Q. Zhang, S.W. Gong, Y. Zhang, T. Yang, C.Y. Wang, N. Gu, Journal of Materials Chemistry 20 (2010) 5110.
[22] H. Wei, E. Wang, Analytical Chemistry 80 (2008) 2250.
[23] A. Asati, S. Santra, C. Kaittanis, S. Nath, J.M. Perez, Angewandte Chemie 121 (2009) 2344.
[24] F. Yu, Y. Huang, A.J. Cole, V.C. Yang, Biomaterials 30 (2009) 4716.
[25] X. Zuo, C. Peng, Q. Huang, S. Song, L. Wang, D. Li, C. Fan, Nano Research 2 (2009) 617.
[26] Y. Miao, H. Wang, Y. Shao, Z. Tang, J. Wang, Y. Lin, Sensors and Actuators B 138 (2009) 182.
[27] Y. Song, K. Qu, C. Zhao, J. Ren, X. Qu, Advanced Materials 22 (2010) 2206.
[28] W. Chen, J. Chen, A.L. Liu, L.M. Wang, G.W. Li, X.H. Lin, ChemCatChem 3 (2011) 1151.
[29] S. Liu, F. Lu, R. Xing, J.J. Zhu, Chemistry: A European Journal 17 (2011) 620.
[30] (a) R. Baron, C.H. Huang, D.M. Bassani, A. Onopriyenko, M. Zayats, I. Willner, Angewandte Chemie International Edition 44 (2005) 4010;
(b) M.A. Fox, M.T. Dulay, Chemical Reviews 93 (1993) 341;
(c) B. Ludolph, M.A. Malik, P. O'Brien, Chemical Communications 8 (1998) 1849.
[31] Z.A. Peng, X.G. Peng, Journal of the American Chemical Society 123 (2001) 183.
[32] X.F. Duan, Y. Huang, R. Agarwal, C.M. Lieber, Nature 421 (2003) 241.
[33] X.F. Duan, C.M. Niu, V. Sahi, J. Chen, J.W. Parce, S. Empedocles, J.L. Goldman, Nature 425 (2003) 274.
[34] D.J. Milliron, S.M. Hughes, Y. Cui, L. Manna, J.B. Li, L.W. Wang, A.P. Alivisatos, Nature 430 (2004) 190.
[35] R. Agarwal, C.J. Barrelet, C.M. Lieber, Nano Letters 5 (2005) 917.
[36] M. Nyman, M.J. Hampden-Smith, E.N. Duesler, Inorganic Chemistry 36 (1997) 2218.
[37] P.S. Nair, T. Radhakrishnan, N. Revaprasadu, G.A. Kolawolea, P. O'Brien, Journal of Materials Chemistry 12 (2002) 2722.
[38] P.S. Nair, T. Radhakrishnan, N. Revaprasadu, G.A. Kolawolea, P. O'Brien, Polyhedron 22 (2003) 3129.
[39] P.S. Nair, G.D. Scholes, Journal of Materials Chemistry 16 (2006) 467.
[40] C. Byrom, M.A. Malik, P. O'Brien, A.J.P. White, Polyhedron 19 (2000) 211.
[41] T.C. Deivaraj, J.H. Park, M. Afzaal, P. O'Brien, J.J. Vittal, Chemistry of Materials 15 (2003) 2383.
[42] M.A. Malik, M. Afzaal, P. O'Brien, Chemical Reviews 110 (2010) 4417.
[43] Z.H. Zhang, W.S. Chin, J.J. Vittal, Journal of Physical Chemistry B 108 (2004) 18569.
[44] G. Malandrino, S.T. Finocchiaro, P. Rossi, P. Dapportob, I.L. Fragala, Chemical Communications (2005) 5681.
[45] T. Zhai, X. Fang, Y. Bando, Q. Liao, X. Xu, H. Zeng, Y. Ma, J. Yao, D. Golberg, Acs Nano 3 (2009) 949.
[46] P. Bera, C.H. Kim, S.I. Seok, Solid State Sciences 12 (2010) 532.
[47] P. Yan, Y. Xie, Y. Qian, X. Liu, Chemical Communications (1999) 1293.
[48] SAINT, version 6.02, SADABS, version 2.03, Bruker AXS Inc., Madison, WI, 2002.
[49] G.M. Sheldrick, SHELXL-97, Program for the Refinement of Crystal Structures, University of Gottingen, Gottingen, Germany, 1997.
[50] SHELXTL, version 6.10, Bruker AXS Inc., Madison, WI, 2002.
[51] L. Spanhel, M. Haase, H. Weller, A. Henglein, Journal of the American Chemical Society 109 (1987) 5649.
[52] W.W. Yu, L. Qu, W. Guo, X. Peng, Chemistry of Materials 15 (2003) 2854.
[53] Z. Zhuang, X. Lu, Q. Peng, Y. Li, Journal of the American Chemical Society 132 (2010) 1819.
[54] G.H. Shen, J.H. Cho, J.K. Yoo, G.C. Yi, C.J. Lee, Journal of Physical Chemistry B 109 (2005) 9294.
[55] B. Liu, G.Q. Xu, L.M. Gen, C.H. Chew, W.S. Li, Z.X. Shen, Journal of Applied Physics 89 (2001) 1059.
[56] Y.W. Jun, S.M. Lee, N.J. Kang, J. Cheon, Journal of the American Chemical Society 123 (2001) 5150.